Available online at www.sciencedirect.com

ScienceDirect

Procedia Structural Integrity 8 (2018) 399–409

Structural Integrity Procedia

www.elsevier.com/locate/procedia

AIAS 2017 International Conference on Stress Analysis, AIAS 2017, 6-9 September 2017, Pisa, Italy

On the homogenization of periodic beam-like structures

Francesco Penta*[a],Luca Esposito[a], Giovanni Pio Pucillo[a], Vincenzo Rosiello[a], Antonio Gesualdo[b],

[a]*Department of Industrial Engineering, University of Naples Federico II, Piazzale Tecchio 80, 80125 Naples, Italy*
[b]*Department of Structures for Engineering and Architecture, University of Naples Federico II, via Claudio 21, 80125 Naples, Italy*

Abstract

A homogenization method for periodic beam-like structures that is based on the unit cell force transmission modes is presented. Its main advantage is that to identify the principal vectors of the state transfer matrix corresponding to the transmission modes it operates directly on the sub-partitions of the unit cell stiffness matrix and allows to overcome the problems due to ill-conditioning of the transfer matrix. As case study, the Pratt girder is considered. Closed form solutions for the transmission modes of this girder are achieved and used into homogenization. Since the pure bending mode shows that the Pratt unit cell transmits two kinds of bending moments, one given by the axial forces and the other originated by nodal moments, the Timoshenko couple-stress beam is employed as substitute continuum. Finally, a validation of the proposed procedure is carried out comparing the predictions of the homogenized models with the results of a series of girder f.e. analyses.

Peer-review under responsibility of the Scientific Committee of AIAS 2017 International Conference on Stress Analysis

Keywords: Pratt and Vierendeel girders; Beam like lattice; Timoshenko couple-stress beam; Homogenization; Force transmission modes; Transfer state matrix eigen-analysis

1. Introduction

Periodic beam-like structures offer the optimal trade-off between strength and stiffness, joined with lightness, economy and manufacturing times. For this reason, they are receiving growing interest from researchers and technicians of several engineering areas and find frequent applications in civil and industrial buildings, naval, aerospace, railways and bridge constructions, material design and bio-mechanics (Salmon et al. (2008); Cao et al (2007); Salehian et al (2006); Cheng et al (2013); Tej and Tejová (2014); Fillep et al (2014); Zhang et al (2016); El Khoury et al (2011); Syerko et al (2013); Ju et al (2008); Kerr (1980); Pucillo (2016); De Iorio et al (2014a - c); De Iorio et al (2017)).

* Corresponding author. Tel.: +39-081-7682451; fax:+39-081-7682466.
E-mail address: penta@unina.it

Peer-review under responsibility of the Scientific Committee of AIAS 2017 International Conference on Stress Analysis
10.1016/j.prostr.2017.12.040

Modelling these structures with a 1-D homogenized continuum model is of great utility in the real problems. While several micropolar models have been reported for the analysis of planar lattices and periodic micro-structures (Noor (1988); Bazant and Christensen (1972); Kumar and McDowell (2004); Ostoja-Starzewski et al (1999); Segerstad et al (2009); Donescu et al (2009); Warren and Byskov (2002); Onck (2002); Liu and Su (2009); Dos Reis and Ganghoffer (2012); Hasanyan and Waas (2016), to cite a few), the studies on the micro-polar models for beam-like lattices have not yet achieved the same advances. As far as the authors are aware, only few papers have specifically addressed this topic (Noor and Nemeth (1980); Salehian and Inman (2010); Romanoff and Reddy (2014); Gesualdo et al (2017)).

In this work, a method for the homogenization of periodic beam-like structures is reported. It is based on the unit cell state transfer matrix eigen-analysis. This technique so far has been applied mostly for the dynamic analysis of repetitive or periodic structures (Mead (1970); Meirowitz and Engels (1977); Zhong and Williams (1995); Langley (1996)). Only recently, it has also been used for the elasto-static analysis of prismatic beam-like lattices with pin-jointed bars (Stephen and Wang (1996); Stephen and Wang (2000); Stephen and Ghosh (2005)). Its practical implementation is problematic since the state transfer matrix $\mathbf{G}$ is defective and ill-conditioned. To overcome ill-conditioning, in Stephen and Wang (2000) two approaches, the force and displacement transfer methods, are presented. By them, a better conditioning is achieved analysing the behaviour of a lattice of *n* identical cells.

The method we propose instead operates directly on the sub-partitions of the unit cell stiffness matrix for searching the unit principal vectors of $\mathbf{G}$ and consequently avoids all the numerical drawbacks of the transfer methods till now proposed. For the simple case of the Pratt girder, closed form solutions for the unit cell force transmission modes are obtained and used to evaluate the stiffnesses of the equivalent Timoshenko micropolar beam. The accuracy of the homogenised medium in reproducing the behaviour of real discrete beam-like structures is finally assessed with a sensitivity analysis carried out by finite element models.

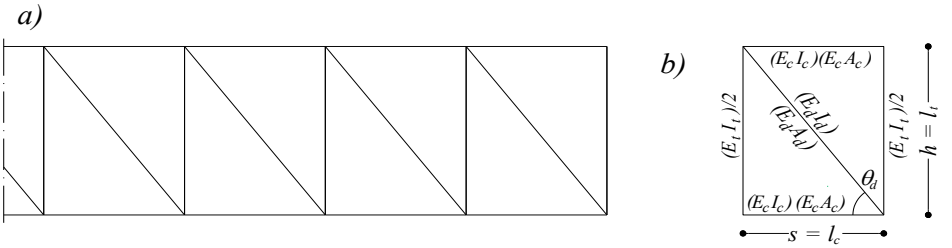

Fig. 1 - Pratt girder (a) and the corresponding unit cell (b)

2. Pratt girder transmission modes

The unit cell of the analysed girder is made up of two straight parallel chords rigidly connected to the webs (see Fig. 1). All the cell members are Bernoulli-Euler beams. The top and bottom chords have the same section whose area and second order central moment are denoted A_c and I_c. To simplify the analysis, the girder transverse webs are assumed axially inextensible. This is equivalent to neglect the transverse elongation among the chords during girder deformation. The cross-sectional area and the second order moment of the diagonal members are A_d and I_d, while I_t denotes the second order moment of the transverse webs. To account the girder periodicity, the two vertical beams of the unit cell will have second order moment equal to the half part of I_t.

To identify any quantity related to the girder *i-th* nodal section, the sub-script *i* will be adopted, see Fig. 2. To distinguish between the joints or nodes of the same section, the superscripts *t* or *p* are used, depending on whether the top or bottom chord is involved. Finally, in a coherent manner, top and bottom nodes of the section *i* are labelled i_t or i_b.

The static and kinematical quantities of the *i-th* cell are schematically shown in Fig. 2. However, for our purposes, it is more convenient to adopt static and kinematic quantities alternative to the standard ones of Fig. 2. More precisely, the deformed shape of the cell will be defined in terms of the mean axial displacement $\hat{u}_j = 1/2\left(u_j^t + u_j^b\right)$, the section rotation $\psi_j = \left(u_j^b - u_j^t\right)/l_t$, the transverse displacement v_j and, finally, the symmetric and anti-symmetric parts of the

section nodal rotations $\hat{\varphi}_j = 1/2\left(\varphi_j^t + \varphi_j^b\right)$ and $\tilde{\varphi}_j = 1/2\left(\varphi_j^t - \varphi_j^b\right)$.

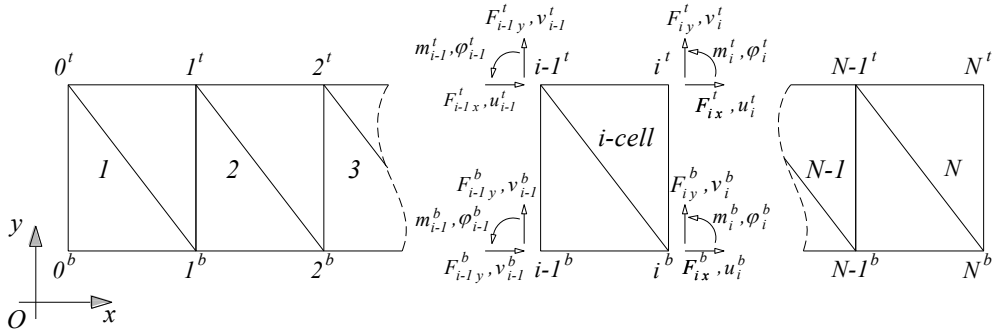

Fig. 2. Unit cell nodes numbering with girder nodal inner forces and displacements

The static quantities conjugates of the previous kinematic variables are: the axial force $n_j = (F_j^b + F_j^t)/2$, the bending moment $M_j = \left(F_j^b - F_j^t\right) l_t$ generated by the anti-symmetric axial forces, the shear force $V_j = F_{jy}^t + F_{jy}^b$, the resultant of the nodal moments $\hat{m}_j = m_j^t + m_j^b$ and, finally, the difference between the same moments $\tilde{m}_j = m_j^t - m_j^b$.

The state vector $\mathbf{s}$ of a girder nodal cross section consists of the displacements and forces vectors $\mathbf{d}$ and $\mathbf{f}$. Hence, the state vectors of the end sections of the *i* cell are $\mathbf{s}_{i-1} = [\mathbf{d}_{i-1}{}^T \quad \mathbf{f}_{i-1}{}^T]^T$ and $\mathbf{s}_i = [\mathbf{d}_i{}^T \quad \mathbf{f}_i{}^T]^T$, Fig. 2. They are related by the transfer matrix $\mathbf{G}$:

$$\mathbf{G}\,\mathbf{s}_{i-1} = \mathbf{s}_i \,.$$

As shown in Stephen and Wang (2000), the force transmission modes of the unit cell are given by the unit principal vectors of the $\mathbf{G}$ matrix. More in particular, the axial transmission mode is the principal vector $\mathbf{s}_a$ generated by the unit eigen-vector of $\mathbf{G}$ defining a rigid axial translation u_a. The unit eigen-vector corresponding to a transversal rigid translation generates instead the in plane rigid rotation principal vector and this latter gives the pure bending transmission mode $\mathbf{s}_b$. Finally, the shear transmission mode $\mathbf{s}_V$ is the principal vector generated by the pure bending mode $\mathbf{s}_b$. Also in the simplest cases, these modes must be determined numerically and for this reason ill-conditioning of $\mathbf{G}$ makes very problematic the practical implementation of the transfer methods.

By the approach proposed in present paper the ill-conditioning problems are altogether avoided since principal vector of $\mathbf{G}$ are determined in closed form by operating directly on the unit cell stiffness matrix. If $\mathbf{s}_e = \left[\mathbf{d}_e^T, \mathbf{f}_e^T\right]^T$ is a unit eigen-vector, the principal vector $\mathbf{s}_p = \left[\mathbf{d}_p^T, \mathbf{f}_p^T\right]^T$ of the $\mathbf{G}$ matrix generated by $\mathbf{s}_e$ is such that $\mathbf{G}\,\mathbf{s}_p = \mathbf{s}_p + \mathbf{s}_e$. The displacement and force sub vectors of $\mathbf{s}_e$ and $\mathbf{s}_p$ are thus linked through the sub-partitions $\mathbf{\Xi}_{ij}$ of the stiffness matrix by the equation:

$$\begin{bmatrix} -\mathbf{f}_p \\ \mathbf{f}_p + \mathbf{f}_e \end{bmatrix} = \begin{bmatrix} \mathbf{\Xi}_{ll} & \mathbf{\Xi}_{lr} \\ \mathbf{\Xi}_{rl} & \mathbf{\Xi}_{rr} \end{bmatrix} \begin{bmatrix} \mathbf{d}_p \\ \mathbf{d}_p + \mathbf{d}_e \end{bmatrix} \tag{1}$$

where subscript l and r are used to denote the left and right side of the unit cell and the matrices $\mathbf{\Xi}_{ij}$ (with $i, j = l, r$) are the four sub-partitions of the cell stiffness matrix (see Appendix **A**). By adding term by term the two equations in (1) and recasting the result in order to have the known terms at left hand side, the next condition for the unknown displacement vector $\mathbf{d}_p$ is deducted:

$$\mathbf{f}_e - \mathbf{B}\mathbf{d}_e = \mathbf{A}\mathbf{d}_p \tag{2}$$

with $\mathbf{A}=\mathbf{\Xi}_{ll}+\mathbf{\Xi}_{lr}+\mathbf{\Xi}_{rl}+\mathbf{\Xi}_{rr}$ and $\mathbf{B}=\mathbf{\Xi}_{lr}+\mathbf{\Xi}_{rr}$. By a very similar reasoning, it can be shown also that unit eigen-vector of $\mathbf{G}$ are such that $\mathbf{A}\mathbf{d}_e=\mathbf{0}$.

Having determined the displacement sub-vector $\mathbf{d}_p$ by solution of eq. (2), the corresponding force sub-vector $\mathbf{f}_p$ can be evaluated by substituting $\mathbf{d}_p$ in the first equation in (1), thus obtaining: $\mathbf{f}_p=-\left(\mathbf{\Xi}_{ll}+\mathbf{\Xi}_{lr}\right)\mathbf{d}_p-\mathbf{\Xi}_{lr}\mathbf{d}_e$.

The $\mathbf{A}$ matrix has some properties that make straightforward the searching of the unit eigen and principal vectors of the $\mathbf{G}$ matrix. Actually, rigid translations of the cell do not produce any force and moment on the cross sections. Then, the vector sums respectively of the first and the sixth columns and of the third and the height columns of the stiffness matrix are equal to the null vectors. Being the matrix symmetric, also the sums of its first and sixth rows and third and eight rows will give the null vectors. Therefore, the $\mathbf{A}$ matrix, that is obtained by adding the four contiguous 5×5 sub-partitions of the stiffness matrix, will systematically have the first and third columns and the first and third rows zero-filled. Furthermore, $\mathbf{A}$ can be viewed as the stiffness matrix of the plane elastic system obtained from the unit cell by introducing the inner constraint conditions: $\mathbf{d}_i=\mathbf{d}_{i+1}=\mathbf{d}$, thus it is symmetric and semi-positive definite.

The principal vector $\mathbf{s}_b$. of the Pratt girder that corresponds to the pure bending mode has displacement sub vector $\mathbf{d}_b$ given by:

$$\mathbf{d}_b=1/2\ [0\quad \varphi\quad 0\quad \varphi\quad \omega\varphi]^T \tag{3}$$

where φ is the rigid unit cell rotation and $\omega=\eta_d/\left(2\eta_t+\eta_d+6\eta_c\right)$, with $\eta_c=E_cI_c/l_c$, $\eta_d=E_dI_d/l_d$ and $\eta_t=E_tI_t/2l_t$. Moreover, the corresponding force sub-vector is:

$$\mathbf{f}_b=\varphi[0\quad 1/2\,\beta_c\quad 0\quad 2\eta_c+\eta_d\left(1-\omega\right)\quad 0]^T \tag{4}$$

with $\beta_c=E_cA_cl_t^2/l_c$.

Concerning the shear transmission mode, the anti-symmetric part $\tilde{\varphi}_V$ of the nodal rotations of the related displacement sub-vector $\mathbf{d}_V$, being uncoupled from the other components, is easily obtained:

$$\tilde{\varphi}_V=\frac{\left(6\eta_c+\eta_d+2\eta_t\right)\omega+\eta_d}{4\left(2\eta_c+\eta_d+2\eta_t\right)}\varphi=\frac{1}{2}\omega\,\varphi.$$

To obtain instead the rotational components ψ_V and $\hat{\varphi}_V$ a $\left(2\times 2\right)$ sub-matrix $\hat{\mathbf{A}}$ of $\mathbf{A}$ has to be inverted and right-multiplied for the column vector formed by the second and fourth row of the known term vector of eq. (2) where $\mathbf{d}_e$ and $\mathbf{f}_e$ are substituted by $\mathbf{d}_b$ and $\mathbf{f}_b$. By this way, the following expressions of ψ_V and $\hat{\varphi}_V$ are derived:

$$\begin{aligned}
\psi_V &= 12\frac{\varphi}{\Delta_p}\left\{\left(2\eta_t+\eta_d\sin^2\theta_d\right)\left[8\,\eta_c+\eta_d\left(3\cos^2\theta_d+2\omega+1\right)\right]+\right.\\
&\left.\left(\eta_c+\eta_d+2\eta_t\right)\left[\frac{\beta_c}{2}+\frac{1}{4}\beta_d\cos^2\theta_d-3\eta_d\sin^2\theta_d\left(\cos^2\theta_d+\omega\right)\right]\right\};\\
\hat{\varphi}_V &= \frac{\varphi}{\Delta_p}\left\{\left(\beta_d\cos^2\theta_d+12\eta_d\sin^4\theta_d+24\eta_t\right)\cdot\left[8\,\eta_c+\eta_d\left(3\cos^2\theta_d+2\omega+1\right)\right]+\right.\\
&\left.+12\left(2\eta_t+\eta_d\sin^2\theta_d\right)\left[\frac{\beta_c}{2}+\frac{\beta_d\cos^2\theta_d}{4}-3\eta_d\sin^2\theta_d\left(\cos^2\theta_d+\omega\right)\right]\right\}
\end{aligned} \tag{5a, b}$$

being $\beta_d=(E_dA_d/l_d)l_t^2$ and $\Delta_p=\left(\beta_d\cos^2\theta_d+12\eta_d\sin^4\theta_d+24\,\eta_t\right)\left(24\eta_c+12\eta_d+24\eta_t\right)-\left(12\eta_d\sin^2\theta_d+24\eta_t\right)^2$.

The algebraic manipulations to determine the force sub-vector $\mathbf{f}_V$ are cumbersome and time-consuming. Besides,

they are not necessary, since the transmitted shear force can be directly evaluated by analyzing the unit cell equilibrium.

Finally, the components $\mathbf{d}_a$ and $\mathbf{f}_a$ of the axial force transmission mode are:

$$\mathbf{d}_a = \frac{u_a}{l_d \sin\theta_d}\left[¿, 1 - 288\,\eta_t \frac{\left(\eta_d \cos^2\theta_d + 2\,\eta_c\right)}{\Delta_p}, ¿, 24\,\eta_t \frac{\left(12\,\eta_d \cos^2\theta_d + \beta_d - 12\,\eta_d\right)\cos^2\theta_d}{\Delta_p}, 0 \right] \tag{6}$$

$$\mathbf{f}_a = \frac{2u_a}{{l_d}^2 \sin^2\theta_d}\left[\beta_c + 144\,\eta_t \frac{\beta_d\left(\eta_d + 2\eta_c\right)\cos^2\theta_d + 24\,\eta_c \eta_d \sin^4\theta_d}{\Delta_p}, 0, 0, 0, 72\,\frac{\beta_d \cos^2\theta_d + 24\eta_c \sin^2\theta_d}{\Delta_p}\eta_t \eta_d\, l_d \sin\theta_d \right] \tag{7}$$

where the symbol ¿ is adopted to denote indeterminate quantities. It is noteworthy that the axial force is transmitted together with symmetric self-equilibrated moments applied at the nodes of each cell end-section. In addition, the unit cell of the Pratt girder deforms also with sectional and symmetric nodal rotations.

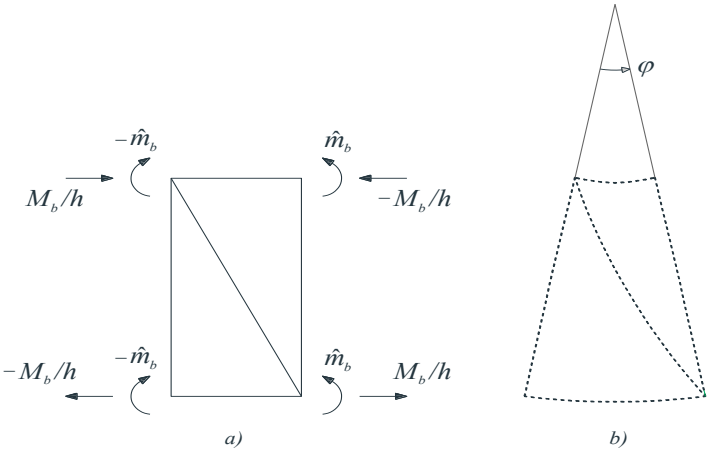

Fig. 3. Pure bending transmission mode: a) components of the force sub-vector $\mathbf{f}_b$, b) unit cell deformed shape.

3. Pratt girder equivalent beam

Analysis of the components of the $\mathbf{f}_b$ vector given in eq. (4) reveals that two bending moments are transferred through the unit cell of the Pratt girders. The first one is generated by the axial forces acting on the nodal cross sections, the other one is due to the moments applied on the joints of the unit-cell and is induced by the bending of chords, webs and diagonal. For this reason, as equivalent continuum, the modified polar Timoshenko beam of Ma et al 2008 is adopted. The homogenized beam stiffnesses are determined by averaging over the unit cell length the cell responses under the load conditions defined by the force transmission principal vectors found in sec. 2. Thus, the equivalent axial stiffness κ_a of the homogenized beam is:

$$\kappa_a = \frac{\hat{n}_a}{\Delta u_a} = \frac{\hat{n}_a}{\hat{u}} \tag{8}$$

where $\hat{n}_a$ is the axial component of the force sub-vector $\mathbf{f}_a$ while $\Delta u_a = \hat{u}$ is the corresponding mean axial elongation

of the unit cell.

The equivalent primary bending stiffness Γ_b is calculated as the ratio of the primary bending moment M_b generated by the axial forces to the mean curvature $1/R$ of the cell. This latter is given by the relative rotation $\Delta\psi_b = \varphi$ of the cell end sections under bending divided by the cell length l_c (Fig. 3). Therefore, we have:

$$\Gamma_b = M_b \cdot R = M_b l_c / \varphi. \tag{9}$$

Secondary bending stiffness Γ_p can be instead evaluated observing that, when the shear force is zero, the polar and Navier moment of the homogenized beam make work by the same generalized strain, namely the beam curvature $d\varphi / dX$. For this reason, we can evaluate the polar bending stiffness as the ratio of the symmetric moment component $\hat{m}_b$ of $\mathbf{f}_b$ and the mean cell curvature:

$$\Gamma_p = \hat{m}_b R = \hat{m}_b l_c / \varphi. \tag{10}$$

Equivalent axial and bending stiffnesses obtained by eq (8) - (10) and the results of section 3 are reported in Tab. I. By inspection of these results it is deduced that primary bending stiffnesses depend only on the chords axial stiffnesses. In addition, axial elongation of the Pratt unit cell is accompanied by rotations both of its joints and end sections. Consequently, its equivalent axial stiffness is dependent also on the bending stiffness of the chords and battens.

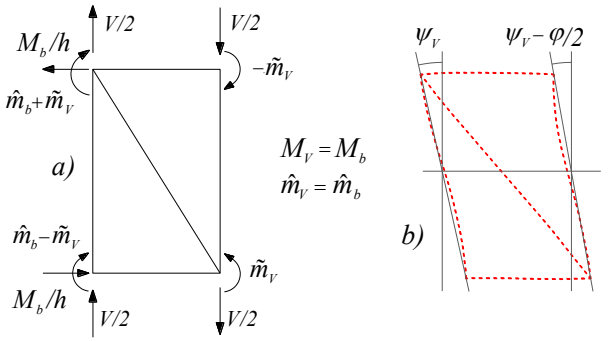

Fig. 4. Shear and bending transmission mode: a) components of the force sub-vectors $\mathbf{f}_v$ and $\mathbf{f}_v + \mathbf{f}_b$ acting on the left and right side of the cell, b) cell deformed shape.

The shear principal vector $\mathbf{s}_V$ is coupled with the pure bending one $\mathbf{s}_V$. The shear force component V of $\mathbf{s}_V$ is given by the condition $-V l_c + M_b + \hat{m}_b = 0$ that defines the in plane rotation equilibrium of the cell. We recall that the displacement sub-vector $\mathbf{d}_V$ is defined up to axial and transversal translations $\hat{u}$ and $\hat{v}$. In Fig. 4 the unit cell deformed shape due to shear and bending is sketched. In this case, the shear angle γ is equal to the average nodal section rotation $\bar{\psi}$ of the cell. Bearing in mind the components of the displacement vector $\mathbf{d}_V$ and $\mathbf{d}_V + \mathbf{d}_b$ defining the deformed configurations of the left and right sections of the cell under shear and bending, the following expression of $\bar{\psi}$ is easily obtained:

$$\bar{\psi} = \psi_v + \frac{1}{2}\psi_b$$

Table I - Equivalent stiffnesses for Pratt girder

Bending stiffnesses:

$$\Gamma_h = \frac{1}{2}\beta_c l_c = \frac{1}{2}E_c A_c\, l_t^2$$

$$\Gamma_p = 2\eta_c l_c + \gamma\,\eta_d l_d = 2E_c I_c + \gamma E_d I_d$$

with $$\gamma = \frac{6E_c I_c \tan\theta_d + 2E_t I_t}{E_d I_d \sin\theta_d + 6E_c I_c \tan\theta_d + 2E_t I_t}\cos\theta_d$$

Axial stiffness:

$$\kappa_a = 2\frac{\beta_c l_c}{l_t^2} + \lambda_1 \frac{\beta_d}{l_t^2} + \lambda_2 \frac{\eta_d}{l_d} = 2E_c A_c + \lambda_1 E_d A_d + \lambda_2 \frac{E_d I_d}{l_d^2},$$

where

$$\lambda_1 = \frac{288}{\Delta_a}\frac{E_t I_t}{l_t}\left(\frac{E_d I_d}{l_d} + 2\frac{E_c I_c}{l_c}\right)\cos^3\theta_d$$

$$\lambda_2 = \frac{6912}{\Delta_a}\frac{E_t I_t}{l_t}\frac{E_c I_c}{l_c}\cos\theta_d \sin^2\theta_d$$

$$\Delta_a = \left(\beta_d \cos^2\theta_d + 12\,\eta_d \sin^4\theta_d + 24\,\eta_t\right)\left(24\,\eta_c + 12\,\eta_d + 24\eta_t\right) - \left(12\,\eta_d \sin^2\theta_d + 24\,\eta_t\right)^2$$

Hence, the equivalent shear stiffness will be:

$$\kappa_V = \frac{V}{\gamma} = 2\frac{M_b + \hat{m}_b}{l_c\left(2\psi_v + \psi_b\right)} \tag{11}$$

The eq. (8) - (11) completely define the elastic behaviour of the equivalent Timoshenko beam. The range of validity of these homogenized equations is analysed in the sec. 5 based on the numerical results of a sensitivity analysis.

4. Validation analysis

The equivalent beam model defined in Section 3, has been validated with a sensitivity analysis involving geometrical and mechanical parameters. The girder responses are deducted via f.e. analysis on cantilevered girders engendered by assembling Bernoulli-Euler beams. Unit vertical load is applied respectively at the free end and at the midpoint. The accuracy of the theoretical predictions has been quantified by the following dimensionless measure of the homogenization error:

$$e\% = 100\frac{\left\|\Delta\mathbf{v}\right\|}{\left\|\mathbf{v}_{FE}\right\|},$$

being $\mathbf{v}_{FE}$ the vector of the vertical displacements of the girder nodal sections obtained by f.e. analysis and $\Delta\mathbf{v} = \mathbf{v}_{\hom} - \mathbf{v}_{FE}$ with $\mathbf{v}_{\hom}$ the nodal vertical displacements vector of the homogenised beam. Furthermore, to have an additional measure of model accuracy and to get also direct indications about the influence exerted on the model equilibrium shapes by the couple-stress bending stiffness, for each examined girder geometry the maximum displacement f of the equivalent model is compared with that f_{FE} of the corresponding f.e. model and the one $\hat{f}$ of the Timoshenko (Cauchy) beam having bending and shear stiffness equal respectively to the primary and shear stiffness of the couple-stress equivalent beam.

Since, as a first approximation, the main parameter influencing the relative importance of the two bending moments acting on the girder cross section is the height h of the girder, in the first set of f.e. analysis the effects of the changes of this parameter have been considered. Under the assumption that both chords and webs have the same cross section, specifically HEA100, cantilever girder f.e. models having height $h=l_t$=300, 600 and 1200 mm, cell aspect ratios $\alpha = l_t/l_c = 0.5, 1$ and 2 and girder aspect ratio $\beta = L/l_t = 6, 12, 24$ and 48 have been examined. Previous values of h, α and β as well the chords and webs cross sections properties were chosen to obtain girders geometries similar to those encountered in the practice of structural design.

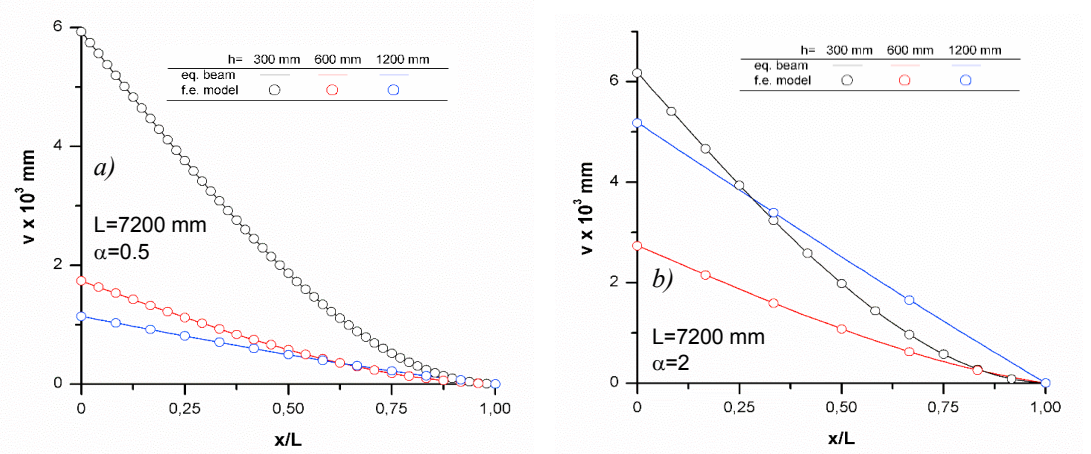

Fig. 5. Deformed shapes of Vierendeel girders for various girder heights: a) cell shape factor $\alpha = l_c/l_t = 0.5$, b) cell shape factor $\alpha = l_c/l_t = 2$ (chords and webs HEA100).

Table II – Pratt girders equivalent stiffnesses, deflections and homogenization errors as function of the diagonal geometry.

	diagonal	Γ_b	Γ_p	κ_V	f_{FE}	f	$\hat{f}$	$e\%$
	[-]	[Nmm]	[Nmm]	[Nmm^{-1}]	[mm]	[mm]	[mm]	[%]
L=7200 mm	80 x 8	9,396E+13	2,702E+12	1,937E+08	9,100E-5	8,932E-5	1,013E-04	1,751
β=12	70 x 7	"	2,619E+12	1,500E+08	9,400E-5	9,197E05	1,068E-04	2,112
	55 x 6	"	2,548E+12	1,035E+08	9,900E-5	9,714E05	1,176E-04	1,571
	30 x 6	"	2,505E+12	5,787E+07	1,130E-4	1,100E04	1,450E-04	2,021

In Fig. 5a, as an example, the deformed shapes of f.e. girders having cell-aspect ratio are compared with those of the corresponding equivalent beams. In Table II, for all the considered geometries, the homogenization errors, the equivalent stiffnesses and the deflections f, f_{FE} and $\hat{f}$ are listed.

A second series of girder models analyse the effects of the changes of diagonal cross-sectional area on the equivalent model accuracy, since the girder shear stiffness is strongly influenced by this geometric parameter. For these analysis, more stout girders have been considered to highlight the shear properties effects in the girder response. For the chords of these models the standard HEA120 section has been chosen. Several back to back angles sections have been considered for the diagonals, while for the battens only the 80×8 back to back angles have been used. The f.e. results and the predictions of the homogenised model are compared in the diagram of Fig. 6b, while in Table III the homogenization errors and the equivalent stiffnesses are reported. In all the examined cases, the model predictions have resulted to be very close to the f.e. outcomes. Thus, the homogenized model is also able to predict the shear dominated girders responses with sufficient accuracy for practical applications.

5. Conclusions

The homogenization of a Pratt girder has been performed adopting a Timoshenko polar beam as substitute medium. The equivalent stiffnesses have been determined by a procedure based on the unit principal vectors of the state transfer matrix of the unit cell. These vectors have been obtained in closed form by a direct method operating on the unit cell stiffness matrix. While in the approaches until now proposed the polar character of the equivalent beam is deduced by kinematical conjectures or is inspired by the micro-structure, in the present study it is a direct consequence of the pattern of the inner forces acting in the lattice when the pure bending mode of the cells is active.

A validation analysis has been carried out on the base of the results of a series of finite element models. In almost all the examined cases the predictions of our model are in good agreement with the numerical outcomes.

The proposed homogenization technique is applicable in several field of structure or mechanical engineering interest. More specifically, it appears to be a serious candidate to analyse the buckling and post-buckling response of periodic beams infinitely long such as the railway track under thermal load (Pucillo (2016)) or to analyse the dynamic isolation of fragile goods in tall buildings (i.e. art objects, see Monaco et al (2014); Gesualdo et al (2017)). Its range of validity is bounded by the hypothesis of linear elasticity. Further research will thus be needed to extend the proposed method also in the elasto-plastic range whereas the response of the unit cell has to be analysed by approximated methods as those reported in Fraldi et al (2010); Fraldi et al (2014) and Cennamo et al (2017).

References

Bazant, Z., Christensen, M., 1972. Analogy between micropolar continuum and grid frameworks under initial stress, Int. J. Solids Struct. 8 (3), 327–346.

Cao, J., Grenestedt, J.L., Maroun, W.J., 2007. Steel Truss/Composite Skin Hybrid Ship Hull. Part I: Design and Analysis, Compos. Part A: Appl. Sci. Manuf. 38 (7), 1755-1762.

Cennamo, C., Gesualdo, A., Monaco, M., 2017. Shear plastic constitutive behaviour for near-fault ground motion, ASCE J. Eng. Mech., 143(9), 04017086.

Cheng, B., Qian, Q., Sun, H., 2013. Steel truss bridges with welded box-section members and bowknot integral joints, Part I: Linear and non-linear analysis, J. Constr. Steel Res. 80, 465-474.

De Iorio, A., Grasso, M., Penta, F., Pucillo, G.P., Pinto, P., Rossi, S., Testa, M., Farneti, G., 2014a. Transverse strength of railway tracks: part 1. Planning and experimental setup, Frattura ed Integrità Strutturale, 30, 478-485.

De Iorio, A., Grasso, M., Penta, F., Pucillo, G.P., Rosiello, V., 2014b. Transverse strength of railway tracks: part 2. Test system for ballast resistance in line measurement, Frattura ed Integrità Strutturale, 30, 578-592.

De Iorio, A., Grasso, M., Penta, F., Pucillo, G.P., Rosiello, V., Lisi, S., Rossi, S., Testa, M., 2014c. Transverse strength of railway tracks: Part 3. Multiple scenarios test field, Frattura ed Integrita Strutturale, 30, 593-601.

De Iorio, A., Grasso, M., Penta, F., Pucillo, G.P., Rossi, S., Testa, M., 2017. On the ballast–sleeper interaction in the longitudinal and lateral directions, Proceedings of the Institution of Mechanical Engineers, Part F: Journal of Rail and Rapid Transit, doi: https://doi.org/10.1177/0954409716682629.

Donescu, S., Chiroiu, V., Munteanu, L., 2009. On the Young's modulus of a auxetic composite structure, Mech. Res. Commun. 36 (3), 294-301.

Dos Reis, F., Ganghoffer, J.F., 2012. Construction of micropolar continua from the asymptotic homogenization of beam lattices, Comput. Struct. 112, 354-363.

El Khoury, E., Messager, T., Cartraud, P., 2011. Derivation of the young's and shear moduli of single-walled carbon nanotubes through a computational homogenization approach, Int. J. Multiscale Comput. Eng. 9 (1), 97-118.

Fillep, S., Mergheim, J., Steinmann, P., 2014. Microscale modeling and homogenization of rope-like textiles, PAMM - Proc. Appl. Math. Mech. 14 (1), 549-550.

Fraldi, M., Gesualdo, A., Guarracino, F., 2014. Influence of actual plastic hinge placement on the behavior of ductile frames, J. Zhejiang Univ-Sci. A 15 (7), 482-495.

Fraldi, M., Nunziante, L., Gesualdo, A., Guarracino, F., 2010. On the bounding of multipliers for combined loading, Proc. R. Soc. A-Math. Phys. Eng. Sci. 466 (2114), 493-514.

Gesualdo, A., Iannuzzo, A., Monaco, M., Penta, F., 2017. Rocking of a rigid block freestanding on a flat pedestal, J. Zhejiang Univ. Sci. A, doi: 10.1631/jzus.A1700061.

Gesualdo, A., Iannuzzo, A., Penta, F., Pucillo, G.P., 2017. Homogenization of a Vierendeel girder with elastic joints into an equivalent polar beam, J. Mech. Mater. Struct., 12(4) 485-504.

Hasanyan, A.D., Waas, A.M., 2016. Micropolar Constitutive Relations for Cellular Solids, J. Appl. Mech. 83 (4), 041001-1:10.

Ju, F., Xia, Z., Zhou, C., 2008. Repeated unit cell (RUC) approach for pure bending analysis of coronary stents, Comput. Meth. Biomech. Biomed. Eng. 11 (4), 419-431.

Kerr, A.D., 1980. An improved analysis for thermal track buckling, Int. J. Non-Linear Mech., 15 (2), 99-114.

Kumar, R.S., McDowell, D.L., 2004. Generalized continuum modeling of 2-D periodic cellular solids, Int. J. Solids Struct. 41 (26), 7399–7422.

Langley, R.S., 1996. A transfer matrix analysis of the energetics of structural wave motion and harmonic vibration, Proc. R. Soc. A-Math. Phys. Eng. Sci. 452 (1950), 1631–1648.

Liu, S., Su, W., 2009. Effective couple-stress continuum model of cellular solids and size effects analysis, Int. J. Solids Struct. 46, 2787–2799.

Ma, H.M., Gao, X.L., Reddy, J.N., 2008. A microstructure-dependent Timoshenko beam model based on a modified couple stress theory, J. Mech.

Phys. Solids 56 (12), 3379–3391.
Mead, D.J., 1970. Free wave propagation in periodically-supported infinite beams, J. Sound Vibr. 13 (2) 181–197.
Meirowitz, L., Engels, R.C., 1977. Response of periodic structures by the z-transform method, AIAA Journal 15 (2), 167–174.
Monaco, M., Guadagnuolo, M., Gesualdo, A., 2014. The role of friction in the seismic risk mitigation of freestanding art objects, Natural Hazards, 73(2), 389-402.
Noor, A.K., 1988. Continuum modeling for repetitive lattice structures, Appl. Mech. Rev. 41 (7), 285–296.
Noor, A.K., Nemeth, M.P., 1980. Micropolar beam models for lattice grids with rigid joints, Comput. Methods Appl. Mech. Eng. 21 (2), 249-263.
Onck, P.R., 2002. Cosserat modeling of cellular solids, C. R. Mecanique 330 (11), 717–722.
Ostoja-Starzewski, M., Boccara, S.D., Jasiuk, I., 1999. Couple-stress moduli and characteristics length of a two-phase composite, Mech. Res. Commun. 26 (4), 387-396.
Pucillo, G.P., 2016. Thermal buckling and post-buckling behaviour of continuous welded rail track, Veh. Syst. Dyn. 54 (12), 1785-1807.
Romanoff, J., Reddy, J.N., 2014. Experimental validation of the modified couple stress Timoshenko beam theory for web-core sandwich panels, Compos. Struct. 111, 130-137.
Salehian, A., Cliff, E.M., Inman, D.J., 2006. Continuum modeling of an innovative space-based radar antenna truss, ASCE J. Aerospace Eng. 19 (4), 227-240.
Salehian, A., Inman, D.J., 2010. Micropolar continuous modeling and frequency response validation of a lattice structure, ASME J. Vibr. Acoust. 132 (1), 011010.
Salmon, G.C., Johnson, J.E., Malhas, F.A., 2008. Steel Structures: Design and Behavior - (5th Edition), Prentice Hall.
Segerstad, P.H. AF, Toll, S., Larsson, R., 2009. Micropolar theory for the finite elasticity of open-cell cellular solids, Proc. R. Soc. A-Math. Phys. Eng. Sci. 465 (2103), 843–865.
Stephen, N.G., Ghosh, S., 2005. Eigenanalysis and continuum modelling of a curved repetitive beam-like structure, Int. J. Mech. Sci. 47 (12), 1854–1873.
Stephen, N.G., Wang, P.J., 1996. On Saint-Venant's principle in pin-jointed frameworks. Int. J. Solids Structures, 33 (1), 79-97.
Stephen, N.G., Wang, P.J., 2000. On transfer matrix eigenanalysis of pin-jointed frameworks, Comput. Struct. 78 (4), 603-615.
Syerko, E., Diskovsky, A.A., Andrianov, I.V., Comas-Cardona, S., Binetruy, C., 2013. Corrugated beams mechanical behavior modeling by the homogenization method, Int. J. Solids Struct. 50 (6), 928-936.
Tej, P., Tejová, A., 2014. Design of an Experimental Prestressed Vierendeel Pedestrian Bridge Made of UHPC, Appl. Mech. Mat. - Trans Tech Publ. 587, 1642-1645.
Warren, W.E., Byskov, E., 2002. Three-fold symmetry restrictions on two-dimensional micropolar materials, Eur. J. Mech. A/Solids 21 (5), 779–792.
Zhang, S., Yin, J., Zhang, H. W., Chen, B.S., 2016. A two-level method for static and dynamic analysis of multilayered composite beam and plate, Finite Elem. Anal. Des. 111, 1-18.
Zhong, W.X., Williams, F.W., 1995. On the direct solution of wave propagation for repetitive structures, J. Sound Vib. 181 (3), 485–501.

Appendix A - Pratt girder stiffness sub-matrices

The (5x5) blocks forming the leading diagonal of the Pratt unit cell stiffness matrix are given by

$$\Xi_{xx}=\begin{bmatrix} 2\frac{\beta_c}{l_d^{\,2}\sin^2\theta_d}+\frac{\beta_d\cos^2\theta_d}{l_d^{\,2}\sin^2\theta_d}+12\frac{\eta_d\sin^2\theta_d}{l_d^{\,2}} & \pm\left(\frac{1}{2}\frac{\beta_d\cos^2\theta_d}{l_d\sin\theta_d}+6\frac{\eta_d\sin^3\theta_d}{l_d}\right) & \frac{\beta_d\cos\theta_d}{l_d^{\,2}\sin\theta_d}-12\frac{\eta_d\sin\theta_d\cos\theta_d}{l_d^{\,2}} \\ \pm\left(\frac{1}{2}\frac{\beta_d\cos^2\theta_d}{l_d\sin(\theta_d)}+6\frac{\eta_d\sin^3\theta_d}{l_d}\right) & \frac{\beta_c}{2}+\frac{1}{4}\beta_d\cos^2\theta_d+3\eta_d\sin^4\theta_d+12\eta_t & \pm\left(\frac{1}{2}\frac{\beta_d\cos\theta_d}{l_d}-6\frac{\eta_d\sin^2\theta_d\cos\theta_d}{l_d}\right) \\ \frac{\beta_d\cos\theta_d}{l_d^{\,2}\sin\theta_d}-12\frac{\eta_d\sin\theta_d\cos\theta_d}{l_d^{\,2}} & \pm\left(\frac{1}{2}\frac{\beta_d\cos\theta_d}{l_d}-6\frac{\eta_d\sin^2\theta_d\cos\theta_d}{l_d}\right) & 24\frac{\eta_c}{l_c^{\,2}}+\frac{\beta_d}{l_d^{\,2}}+12\frac{\eta_d\cos^2\theta_d}{l_d^{\,2}} \\ \pm\left(-6\frac{\sin\theta_d\eta_d}{l_d}\right) & -3\eta_d\sin^2\theta_d-12\eta_t & \pm\left(12\frac{\eta_c}{l_c}+6\frac{\eta_d\cos\theta_d}{l_d}\right) \\ 6\frac{\sin\theta_d\eta_d}{l_d} & \pm\left(3\eta_d\sin^2\theta_d\right) & -6\frac{\eta_d\cos\theta_d}{l_d} \end{bmatrix}$$

$$\begin{bmatrix} \pm\left(-6\frac{\eta_d\sin\theta_d}{l_d}\right) & 6\frac{\eta_d\sin\theta_d}{l_d} \\ -3\eta_d\sin^2\theta_d-12\eta_t & \pm\left(3\eta_d\sin^2\theta_d\right) \\ \pm\left(12\frac{\eta_c}{l_c}+6\frac{\eta_d\cos\theta_d}{l_d}\right) & -6\frac{\eta_d\cos\theta_d}{l_d} \\ 8\eta_c+4\eta_d+12\eta_t & \pm\left(-4\eta_d\right) \\ \pm\left(-4\eta_d\right) & 4\eta_d+8\eta_c+4\eta_t \end{bmatrix},$$

with $x=l,r$ and where $\eta_c=E_cI_c/l_c$, $\eta_d=E_dI_d/l_d$, $\eta_t=E_tI_t/l_t$, $\beta_c=E_cA_cl_t^2/l_c$ and $\beta_d=E_dA_dl_t^2/l_d$. For the components of Ξ_{xx} affected by the $\pm$, the upper sign is for $x=l$, the lower for $x=r$. Furthermore, for the upper and lower out-diagonal blocks it results:

$$\Xi_{lr}=\Xi_{rl}^{T}=\begin{bmatrix} -2\frac{\beta_c}{l_d^{\,2}\sin^2\theta_d}-\frac{\beta_d\cos^2\theta_d}{l_d^{\,2}\sin^2\theta_d}-12\frac{\eta_d\sin^2\theta_d}{l_d^{\,2}} & \frac{1}{2}\frac{\beta_d\cos^2\theta_d}{l_d\sin\theta_d}+6\frac{\eta_d\sin^3\theta_d}{l_d} & -\frac{\beta_d\cos\theta_d}{l_d^{\,2}\sin\theta_d}+12\frac{\eta_d\sin\theta_d\cos\theta_d}{l_d^{\,2}} \\ -\frac{1}{2}\frac{\beta_d\cos^2\theta_d}{l_d\sin\theta_d}-6\frac{\eta_d\sin^3\theta_d}{l_d} & -\frac{\beta_c}{2}+\frac{1}{4}\beta_d\cos^2\theta_d+3\eta_d\sin^4\theta_d & -\frac{1}{2}\frac{\beta_d\cos\theta_d}{l_d}+6\frac{\eta_d\sin^2\theta_d\cos\theta_d}{l_d} \\ -\frac{\beta_d\cos\theta_d}{l_d^{\,2}\sin\theta_d}+12\frac{\eta_d\sin\theta_d\cos\theta_d}{l_d^{\,2}} & \frac{1}{2}\frac{\beta_d\cos\theta_d}{l_d}-6\frac{\eta_d\sin^2\theta_d\cos\theta_d}{l_d} & -24\frac{\eta_c}{l_c^{\,2}}-\frac{\beta_d}{l_d^{\,2}}-12\frac{\eta_d\cos^2\theta_d}{l_d^{\,2}} \\ 6\frac{\eta_d\sin\theta_d}{l_d} & -3\eta_d\sin^2\theta_d & -12\frac{\eta_c}{l_c}-6\frac{\eta_d\cos\theta_d}{l_d} \\ -6\frac{\eta_d\sin\theta_d}{l_d} & 3\eta_d\sin^2\theta_d & 6\frac{\eta_d\cos\theta_d}{l_d} \end{bmatrix}$$

$$\begin{bmatrix} -6\frac{\eta_d\sin\theta_d}{l_d} & -6\frac{\eta_d\sin\theta_d}{l_d} \\ -3\eta_d\sin^2\theta_d & -3\eta_d\sin^2\theta_d \\ 12\frac{\eta_c}{l_c}+6\frac{\eta_d\cos\theta_d}{l_d} & 6\frac{\eta_d\cos\theta_d}{l_d} \\ 4\eta_c+2\eta_d & 2\eta_d \\ -2\eta_d & 4\eta_c-2\eta_d \end{bmatrix}.$$